

Realization and characterization of an all-bands-flat electrical lattice


Noah Lape¹,^{*} Simon Diubenkov¹, L. Q. English^{1,*}, P. G. Kevrekidis^{2,†}, Alexei Andreanov^{3,4,‡},
Yeongjun Kim^{3,§} and Sergej Flach^{3,4,||}

¹*Department of Physics and Astronomy, Dickinson College, Carlisle, Pennsylvania 17013, USA*

²*Department of Mathematics and Statistics, University of Massachusetts, Amherst, Massachusetts 01003, USA*

³*Center for Theoretical Physics of Complex Systems, Institute for Basic Science, Daejeon 34126, Republic of Korea*

⁴*Basic Science Program, Korea University of Science and Technology, Daejeon 34113, Republic of Korea*

 (Received 2 September 2025; revised 24 October 2025; accepted 27 October 2025; published 17 November 2025)

We construct an electrical all-bands-flat (ABF) lattice and experimentally generate compact localized states (CLSs) therein. The lattice is a diamond (rhombic) chain and implemented as a network of capacitors and inductors, as well as voltage inverters (using operational amplifiers) in order to introduce a π flux within each diamond. The network's normal modes split into three flat bands, and the corresponding CLSs can be excited in isolation via a two-node driving at the flat-band frequencies. We also examine the role of the lattice edges and their interaction with the CLSs. Finally, we compare the experimental results to tight-binding predictions and obtain very good agreement. This analysis paves the way for further experimental implementations of ABF systems in electric networks, especially with an eye towards exploring their interplay with nonlinearity.

DOI: [10.1103/1w5c-nsmh](https://doi.org/10.1103/1w5c-nsmh)

I. INTRODUCTION

Flat-band systems are tight-binding lattices in which one or more energy bands are dispersionless, e.g., perfectly flat [1–4]. In flat bands transport is completely suppressed even without disorder, leading to compact localization (for finite-range hopping). The macroscopically degenerate eigenstates of a flat band can take the form of conventional plane waves due to the translational symmetry, but they may also manifest as spatially compact, localized states known as compact localized states (CLSs). It is straightforward to obtain CLSs from transformations using combinations of plane wave eigenstates and vice versa.

CLSs have been sought in a variety of contexts, including photonic lattices [5–10], polaritonic systems [11,12], and electrical chains [13–17], among others. As an important variation on the theme, the introduction of interactions [18–27], disorder [28–32], or external magnetic fields [33] in flat bands can induce nonperturbative, nontrivial phenomena, including the formation of compact nonlinear discrete states (such as breathers and standing waves) [8,34,35], or the emergence of symmetry-breaking (or symmetry-restoring) bifurcations [9,36].

The absence of dispersion relies on fine tuning of coupling interactions to suitably induce destructive interference. To understand the underlying mechanisms that give rise to flat bands, multiple flat-band generators for various lattice geometries based on different construction principles have been proposed [37–41]; see, e.g., the detangling approach in

Ref. [42] and the constructive methodology in Ref. [43]. Such dispersionless features are particularly important in shaping the transport and overall dynamical properties of flat-band lattices, justifying the particular interest in them [1,2].

Experimentally, it is often challenging to observe direct evidence of flat bands through the observation of CLSs because that requires preparing (tuning) and observing the precise phase of the wave function in artificial lattice systems. Nevertheless, significant recent progress was reported in Refs. [6,14,44]. Electrical circuits have become a particularly attractive test bed for artificial lattice engineering [45,46]. With only a few passive elements—capacitors, inductors, and diodes—one can build linear and nonlinear lattices that can support flat-band linear spectra, as well as nonlinear solitonic excitations [47–49]. Adding active elements such as operational amplifiers (op-amps), one can, moreover, achieve tunable complex hopping phases, topological band structures, \mathcal{PT} symmetry [50], nonlinearity [17], and even interacting two-particle setups [16]. A scheme using only active elements has also been implemented [51]. The versatility of electric circuits renders them a natural setting to realize flat bands and probe nonperturbative effects, such as interactions, nonlinearities, and disorder [16,17].

Creating an all-bands-flat (ABF) lattice is more challenging compared to a single flat band because of the higher degree of fine tuning of the Hamiltonian, also possibly requiring complex hoppings and, consequently, higher sensitivity to perturbations. In an earlier realization of an ABF lattice using circuits [14], negative hoppings were realized by duplicating the network nodes and interconnecting them, a common approach for synthetic gauges [45].

In this paper we realize a particular ABF model in an electrical circuit. More specifically, herein, we examine a diamond chain with π flux, which is crucially different from our earlier work [17]. The fundamental underlying difference is that this constitutes a model which is known to be an ABF model,

*Contact author: englishl@dickinson.edu

†Contact author: kevrkid@umass.edu

‡Contact author: aalexei@ibs.re.kr

§Contact author: yeongjun.kim.04@gmail.com

||Contact author: sflach@ibs.re.kr

a particular extreme case of flat bands in which all bands are flat [52]. Compared to systems with a single flat band, ABF lattices require more fine tuning, particularly hoppings with different signs, resulting in modeling nonzero effective magnetic flux which penetrates individual plaquettes. Such systems have only very recently started to be experimentally implemented, most notably in the photonic realm [53–56] and in electrical [14] or superconducting [57] circuits. Hence, further experimental platforms enabling their observation would offer considerable additional insights, including the future promise of exploration of the interplay of an ABF linear spectrum and nonlinearity.

We implement a different and simpler circuit than Ref. [14] to create a “ π flux,” i.e., negative hoppings, using an inverting amplifier circuit with op-amps. Our realization of ABF is validated through the observation of CLSs using a resonance via local sinusoidal driving targeted at the flat-band frequencies. We observe a resonance response that is strongly localized on and near the driven site and remains spatially compact throughout the lattice. In addition to identifying the ABF CLS eigenmodes experimentally, we have developed a theoretical framework for modeling the corresponding lattice and have observed very good qualitative and quantitative agreement with the experimental results. This enhances our confidence that the present framework may prove to be a fertile one for future studies.

Our presentation below is structured as follows. In Sec. II we formulate the relevant experimental system and explain how the presence of the op-amps allows for the practical implementation of the “negative coupling.” The theoretical analog of the model is introduced. In Sec. III we present our experimental results on the frequencies and profiles of the CLS modes and corroborate these findings theoretically. Finally, in Sec. IV we summarize our findings and present our conclusions.

II. EXPERIMENTAL SYSTEM AND MODEL

We study a diamond chain: a one-dimensional lattice composed of a chain of plaquettes (rhombuses) in which neighboring ones share common corner nodes. Each unit cell contains three sites (voltages; T_n, U_n, V_n), as shown in Fig. 1(a), where one hopping per plaquette carries a phase ϕ , ensuring a ϕ flux threading each plaquette. Here, black and red edges represent hoppings t and $te^{i\phi}$, respectively.

The tight-binding Hamiltonian reads

$$\hat{H}(\phi) = t \sum_n \hat{T}_n^\dagger (\hat{U}_{n-1} + \hat{V}_{n-1} + e^{i\phi} \hat{U}_n + \hat{V}_n) + \text{H.c.}, \quad (1)$$

where \hat{X}_n^\dagger is the creation operator on sublattice X_n . Setting $\phi = \pi$ makes the red edges real negative, $te^{i\phi} = -t$. Thus, if a single diamond is traversed in a clockwise loop, a phase of π accumulates—a hallmark of an Aharonov-Bohm cage [58–60]. By direct diagonalization, it can be shown that at π flux, all eigenvalues are k independent, producing an ABF spectrum $E = \{0, \pm 2t\}$ with CLSs spanning two unit cells, as shown in Fig. 1(a) [58].

In the electrical circuit network analog of the tight-binding model, the sites (nodes) represent LC resonators, and hoppings (edges) represent inductors that couple two resonators

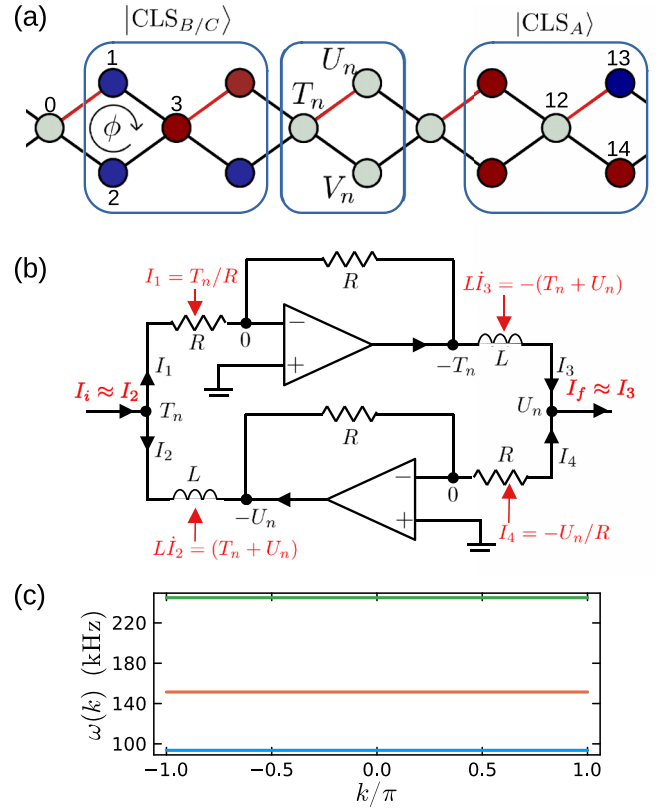


FIG. 1. (a) Tight-binding representation of the basic diamond lattice, with its three-point basis, U_n, V_n, T_n ; also shown is our node numbering scheme. The CLSs for the upper and lower flat bands (among the three FBs) are denoted as $|CLS_{B/C}\rangle$: The B/C CLSs have different amplitudes at the central site and peripheral sites (see main text). The CLS for the middle flat band $|CLS_A\rangle$ is characterized by a vanishing amplitude at the center site (site 12). In the context of the electrical circuit, circles represent LC resonators, black lines depict inductors that couple two resonators, and red lines represent negative inductive coupling. (b) Negative coupling is achieved through voltage inverters, here using op-amps. In (a), we see that the connection between T_n and U_n is negative; the red line is a placeholder for this circuit, explained in more detail in the text. (c) Band structure (in kHz) obtained with parameters specified in Sec. III. Three bands are located at 94 kHz (blue), 151 kHz (red), and 245 kHz (green).

in Fig. 1(a). Here, red lines now represent negative inductive couplings. For the experimental implementation of the ABF lattice, we modified the electrical diamond lattice described in Ref. [17]. The key modification involves periodically introducing π -phase shifts by electrically implementing negative coupling edges.

The design of such a negative edge is shown in Fig. 1(b), where the two nodes T_n and U_n are to be negatively coupled. If these two nodes were connected by a single (ordinary) inductor, the current I flowing from the left to the right node would be governed by $LI = (T_n - U_n)$. We would like to modify this equation to read $LI_f = (-T_n - U_n)$, where I_f denotes the total current flowing into node U_n . This is accomplished by the top branch of the parallel circuit in Fig. 1(b). The voltage at the two ends of the inductor (top right) has values of $-T_n$ and U_n due to the inverting amplifier of unity gain. The resistors

connecting the inverting input node ($-$) of the op-amp and the one at the feedback loop which connects the output inverting node are of equal value R . As we will argue shortly, the resistance R must also be sufficiently large. The negative coupling needs to be bidirectional. In other words, the current I_i flowing out of the T_n node obeys $LI_i = (T_n + U_n)$. This is accomplished by the lower branch of the parallel circuit.

The two currents I_i and I_f do not interfere with one another because the input impedance of this inverter is given by the resistance R of the resistors, and this value is chosen to be much larger than the impedance of the inductor $R \gg |i\omega L|$, where ω is the driving frequency. When this condition is met, very little current originating, for example, from the output of the lower op-amp is diverted to the upper branch and flows (almost) entirely into node T_n , i.e., $I_i \approx I_2$ in Fig. 1(b). Furthermore, for practical reasons, additional resistors R_G are used to connect every noninverting op-amp input to the ground (not shown) [61].

The sites in Fig. 1(a) represent LC resonators, i.e., a parallel combination of an inductor and a capacitor connecting the node to the ground. We can choose their inductance to be infinitely large (open circuit), as justified below in Eq. (3), so that each LC site reduces to a single capacitor C . Thus, the lattice is characterized by only one capacitance value C of the nodes to the ground and one inductance value L of the coupling between nodes. Applying Kirchhoff's voltage law at each node, we arrive at a system of linear differential equations of the form [17]

$$\begin{aligned} \ddot{T}_n + (4\omega_0^2)T_n &= \omega_0^2(U_{n-1} - U_n + V_{n-1} + V_n), \\ \ddot{U}_n + (2\omega_0^2)U_n &= \omega_0^2(T_{n+1} - T_n), \\ \ddot{V}_n + (2\omega_0^2)V_n &= \omega_0^2(T_n + T_{n+1}), \end{aligned} \quad (2)$$

where $\omega_0^2 = 1/(LC)$.

Equations (2) describe the dynamics of the ABF lattice. Using the Bloch-wave ansatz, $U_n = U(k) \exp[i(\omega t - kn)]$ (with similar notation for V_n and T_n), we obtain the eigenvalue equation for the ABF Hamiltonian in reciprocal Bloch space:

$$-\frac{\omega^2}{\omega_0^2} \vec{\psi}(k) = [H(k, \phi = \pi) - D] \vec{\psi}(k), \quad (3)$$

where

$$H(k, \phi) = t \begin{pmatrix} 0 & e^{i\phi} + e^{-ik} & 1 + e^{-ik} \\ e^{-i\phi} + e^{ik} & 0 & 0 \\ 1 + e^{ik} & 0 & 0 \end{pmatrix}$$

is the Bloch Hamiltonian in Eq. (1). Here, the diagonal terms (on-site potentials) $D = \text{diag}(4, 2, 2)$ reflect the number of inductors coupled to sites T_n , U_n , and V_n and ensure $\omega^2 > 0$. Note that unlike the conventional chiral diamond chain [2,43], unequal diagonal terms are present, yet the spectrum remains dispersionless. While the chiral symmetry is formally broken due to the presence of nonzero diagonal terms, a frequency gauge can remove the diagonal terms for the majority sublattice U , V , and therefore, the middle flat band is still protected by partial chiral symmetry [17,62].

Note that a finite on-site inductance L_0 at a site of the LC resonator results in a shift of the resonance frequency of that site by $\omega_0^2(L/L_0)$, which appears as an additional on-site potential term in Eq. (2). If needed, one can also add site-dependent on-site inductances to tune the on-site potential of the model at each site. This may be useful for future studies exploring the interplay of disorder through ‘‘impurity nodes’’ on the ABF lattice, generalizing earlier such studies of regular electrical lattices (see, e.g., [63]). In our case, this tuning is not needed since Eq. (3) already describes an ABF lattice, without additional on-site potential tuning.

Solving the eigenvalue problem yields three eigenvalues:

$$\omega_A = \sqrt{2} \omega_0, \quad \omega_{B/C} = (\sqrt{3 \pm \sqrt{5}}) \omega_0. \quad (4)$$

Note the absence of k in these expressions and hence the existence of three flat bands.

The CLSs of each flat band are shown in Fig. 1(a). Every CLS occupies two unit cells, forming an X shape with four peripheral sites U_n, V_n, U_{n+1} , and V_{n+1} and a central one located between them at the T_n site. For the middle flat band, the amplitude at the center site is zero due to the partial chiral symmetry associated with the flat band. On the other hand, for CLSs of the lower and upper flat bands, the central site and the peripheral sites are simultaneously nonzero. The ratio of the amplitudes at the central site vs the left peripheral sites [sites 1 and 2 in Fig. 1(a)] is $(\sqrt{5} \pm 1)$ for ω_B and ω_C , respectively. For ω_B , the CLS (corresponding to the lower flat bands), $\{U_{n-1}, V_{n-1}\}$, and V_n are in phase with the T_n site, while for ω_C (corresponding to the upper flat bands), they are antiphase with respect to T_n . In all cases, the voltages $\{U_{n-1}, V_{n-1}\}$ of the left pair are in phase with each other, whereas those of the right pair, $\{U_n, V_n\}$, are in antiphase with each other.

III. EXPERIMENTAL RESULTS

In our setup, we use $L = 470 \mu\text{H}$ and $C = 4.7 \text{ nF}$. The resistances of the op-amps are chosen to be $R = 10 \text{ k}\Omega$, ensuring $\omega L \ll R$ for frequencies ω , which is an important criterion, as discussed before (note that $R_G = R/2 = 5 \text{ k}\Omega$). We use LF411 op-amps. This results in the following predictions for three flat-band frequencies: 94, 151, and 245 kHz [Fig. 1(c)].

To probe the CLS, the lattice is driven by a signal generator at one or two sites via small coupling capacitors ($C_d = 3.5 \text{ pF} \ll C$) [17]. Driving at two sites enables the isolation of a single CLS in this system. Spectra are recorded by sweeping the drive frequency and measuring the response at a nearby site, while spatial profiles are captured simultaneously across all nodes using fast data acquisition boards (National Instruments 6133 cards, 2.5 MHz sampling). The detailed spatiotemporal resolution of the relevant system is one of the advantages of the present setting. As was shown in Ref. [17] via a transfer function analysis, once the drive frequency coincides with a flat-band eigenvalue, the response of the entire network localizes to the CLS that involves the driven sites. It is easy to see from the structure of the CLS [Fig. 1(a)] that driving two sites U_n and V_n in-phase and out-of-phase isolates a single CLS: in-phase driving at U_n and V_n excites the

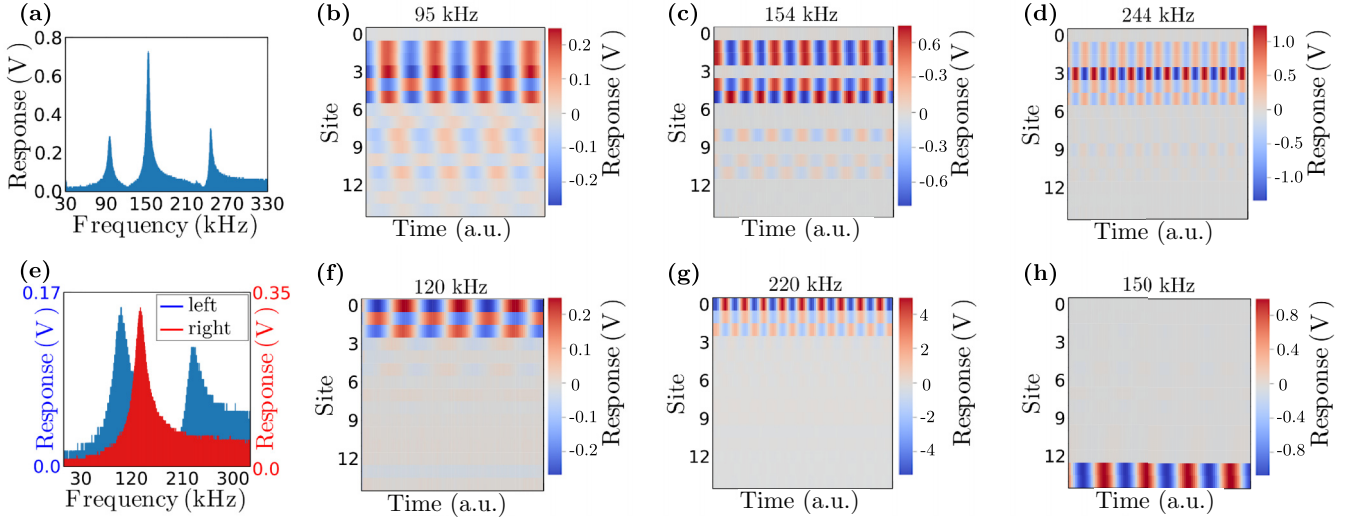


FIG. 2. (a)–(d) The ring lattice with periodic boundary conditions is driven at left-edge nodes 1 and 2 (U_0, V_0) in phase and observed at V_0 . [See Fig. 1(a) for site labeling.] (a) The response at V_0 vs frequency. The spectrum shows three prominent peaks at 95, 154, and 244 kHz. (b)–(d) The full spatiotemporal signature of the CLSs at steady state under sinusoidal driving at $f = 95, 154$, and 244 kHz, respectively. The time window (x axis) ranges from 20 to 50 μ s, capturing 3–10 oscillations ($3/f$ – $10/f$) at steady state. (e) The blue shading shows the frequency response when driving left-edge nodes 1 and 2 (U_0 and V_0) antiphase and observing at node 2. Two peaks appear at 120 and 220 kHz, in good agreement with the edge state eigenvalue calculation. The red shading shows the response when driving right-edge nodes 13 and 14 (U_4 and V_4) in phase. (f)–(h) The full spatiotemporal signature of the CLSs at steady state under sinusoidal driving at the left edge for $f = 120, 220$ kHz and at the right edge for 244 kHz, respectively.

CLS over cells from n to $(n + 1)$, whereas antiphase driving addresses the CLS over cells from $(n - 1)$ to n . In this way, even though we are exciting only a single pair of (U_n, V_n) , we uniquely select a CLS mode pertaining to the suitable ABF model associated with the drive frequency.

A. Excitations in the bulk

We first study a ring (periodic boundary conditions) of five unit cells by connecting nodes 13 and 14 to node 0 in Fig. 1(a). We then inject a sinusoidal signal from a signal generator in sweep mode into one or two nodes of the lattice via a small coupling capacitor ($C_d = 35$ pF). The drive amplitude was varied between 1 and 10 V, which lies well within the components' specified operating ranges, ensuring a linear response throughout the experiment.

Figure 2(a) shows the resulting spectrum from two-node driving (the pair of nodes, U_n, V_n , is driven in phase via two different coupling capacitors). Three clear resonance peaks can be seen at 95, 154, and 244 kHz, which match the above theoretical prediction for flat-band frequencies very well. Single-node driving yields a very similar result in this configuration. The broadening of the peaks is primarily due to the *effective series resistance* $R_{\text{eff}} \approx 20 \Omega$ from the inductors, as analyzed previously in Ref. [17].

Now that the flat-band frequencies have been experimentally ascertained and verified, we can use the signal generator at a fixed frequency to probe the lattice at those three frequencies sequentially. Here, we would like to capture the full spatiotemporal lattice dynamics by recording the voltage responses at each node, using the fast DAQ boards. We start with the lowest flat-band frequency of 95 kHz, shown in Fig. 2(b). It depicts roughly four periods on the horizontal time axis;

the color encodes the voltage, and the vertical axis indexes the lattice nodes (space), using the numbering convention of Fig. 1(a). It is evident that the profile is spatially localized over two unit cells, and we identify it as the CLS corresponding to this lowest flat band.

Similarly, Fig. 2(c) depicts the spatial lattice response at the second flat-band frequency of 154 kHz. Again, the driver was injected at nodes 1 and 2. This CLS mode is characterized by a vanishing amplitude at the center T site (site 3), with the $\{U, V\}$ nodes to the left oscillating in phase and the $\{U, V\}$ nodes to the right oscillating in antiphase. Finally, Fig. 2(d) shows the spatial signature at the highest flat-band frequency of 244 kHz. In contrast to the previous configuration, here the T site (site 3) is highly excited, as expected from the previously discussed theoretical prediction of the CLS. Furthermore, site 3 and sites 1, 2, and 4 are antiphase with each other, which is expected from the tight-binding calculation.

We briefly comment on the quantitative quality of the data. We use three metrics to assess data quality. (1) $r = |T_n/\bar{X}_n|$ is the absolute amplitude ratios of central site and peripheral sites, compared with the theory described in Sec. II. Here, $\bar{X}_n = \sum_{X_{n'} \in S - \{T_n\}} |X_{n'}|/4$ is the mean absolute amplitude over the set S of the CLS sites ($S = \{U_0, V_0, T_1, U_1, V_1\}$). (2) $\tilde{\sigma} = (\sigma_{S - \{T_1\}}/A \times 100)\%$ are the absolute amplitude deviations at the peripheral sites, which are expected to be zero in theory. (3) $\text{SNR} = A/\sigma_{S^c}$ is the signal-to-noise ratio outside the CLS, with S^c averaged over time and sites. Here, A is the maximum amplitude of the CLS.

At 95 kHz (theory: 94 kHz), we obtain $r = 1.23$ (theory: $r = \sqrt{5} - 1 \approx 1.24$), $\tilde{\sigma} = 6\%$, and $\text{SNR} \approx 15$. At 154 kHz (theory: 151 kHz), we obtain $r = 0.009$ (theory: 0), $\tilde{\sigma} = 6\%$, and $\text{SNR} \approx 100$. At 244 kHz (theory: 245 kHz), we obtain $r = 3.2$ (theory: $r = \sqrt{5} + 1 \approx 3.2$), $\tilde{\sigma} = 5\%$, and

SNR ≈ 130 . At 95 kHz the SNR is lower than for the other flat-band resonances. Here, $T_n \approx -1.2U_n$, which reduces the current of I_4 and I_2 at the input and output currents of the negative inductive coupling, $I_f = I_3 + I_4$ and $I_i = I_1 + I_2$. The shorthand $I_f \approx I_4$ and $I_i \approx I_2$ remains valid for large R but is less accurate, and the residual background becomes more visible.

B. Excitations at the edges

Let us now cut the ring lattice to form a line with open boundary conditions. Note that the hopping terms that originally connected node 0 to nodes 13 and 14 should not be simply terminated; they should be connected to the ground to ensure the correct on-site potential at node 0 [e.g., Eq. (2)]. Similarly, the hopping terms that originally connected nodes 13 and 14 to node 0 should be connected to the ground.

If we drive U_0 and V_0 (nodes 1 and 2) in phase (the left edge), we excite a bulk CLS away from the edge, so the edge has no effect. By contrast, if we drive nodes 1 and 2 antiphase, the CLS impinges on the edge. Tight-binding calculations predict two edge states at frequencies 120 and 232 kHz. These states are also compactly localized, occupying sites T_0 , U_0 , and V_0 (nodes 0, 1, and 2), with U_0 and V_0 oscillating antiphase.

The blue shading in Fig. 2(e) illustrates the frequency response of antiphase left-edge driving. Two prominent peaks are observed at 120 and 220 kHz, which agrees well with the tight-binding calculation. Figures 2(f) and 2(g) are the spatiotemporal steady-state profiles of the CLSs at those peaks, which show that they are compactly localized in space at (T_0 , U_0 , and V_0 ; nodes 0, 1, and 2), as expected. Furthermore, by comparing the results to Figs. 2(b) and 2(c), we see that the patterns resemble truncated CLSs; the lower-frequency peak maps to the truncated acoustic CLS, whereas the higher-frequency peak maps to the truncated optic CLS. The difference between them is simply whether sites U_0 and V_0 (sites 0 and 1), which are connected via negative coupling, are oscillating in phase or out of phase.

Next, we consider the right edge. Tight-binding calculations predict a single compactly localized edge mode localized on sites U_n and V_n at the frequency of the middle flat band, 152 kHz. Again, antiphase driving produces a CLS that extends into the bulk, away from the edge, so the edge has no effect. The red shading in Fig. 2(e) shows the frequency response at U_4 (node 13) when two sites, U_4 and V_4 (nodes 13 and 14), are driven in phase. When driving two nodes in phase, we observe one prominent peak at 150 kHz, as predicted from the tight-binding calculation. The spatial profile of the edge state is shown in Fig. 2(h). Only nodes 13 and 14 are oscillating in phase, namely, the ones that are driven. Such a pattern is also accomplished via single-node driving at this frequency. If only site 13 or 14 is driven at that frequency, the same pattern is established.

We perform an analysis analogous to that in Sec. III A, with the only change being that the peripheral set comprises two sites rather than four. In the tight-binding calculation, we enforce zero amplitude on the edge unit cells by imposing destructive-interference boundary conditions— $\{U, V\}$ is in phase on the left edge and antiphase on the right edge—and

then solve a 3×3 eigenvalue problem. At 120 kHz (theory: 120 kHz), we obtain $r = 0.74$ (theory: $r = \sqrt{3} - 1 \approx 0.73$), $\tilde{\sigma} = 0.5\%$, and SNR ≈ 100 . At 232 kHz (theory: 232 kHz), we obtain $r = 2.89$ (theory: $r = \sqrt{3} + 1 \approx 2.73$), $\tilde{\sigma} = 7\%$, and SNR ≈ 62 . At 150 kHz (theory: 152 kHz), we obtain $r = 0.09$ (theory: $r = 0$), $\tilde{\sigma} = 8\%$, and SNR ≈ 150 .

IV. CONCLUSIONS AND FUTURE CHALLENGES

We demonstrated the implementation of a π -flux diamond chain with all bands flat using electric circuits by devising negative inductive coupling that realizes negative hoppings. The key properties of the ABF model were observed: complete absence of dispersion, as evidenced by the lack of band curvature; k -independent resonant modes with compactly localized spatial profiles (CLSs); and Aharonov-Bohm caging, as anticipated from the theory, with very good agreement between the two. We also showed that the electrical systems at hand showcase the relevant phenomenology of flat bands not only at the bulk but also through suitably tailored predictions at the level of surface excitations, e.g., with homogeneous Dirichlet boundary conditions (i.e., experimental “grounding”) at the left or/and right boundary.

Our experiment demonstrates the promising potential of electrical circuit networks as a simple, straightforward tunable platform to set and to spatiotemporally monitor modern band theory, including flat bands: it can realize synthetic magnetic fluxes by inducing phase shifts (here, a π shift), demonstrating the capability of realizing a complicated, fine-tuned, tight-binding network such as an ABF one. We believe that any flux other than π can also be realized using op-amps by implementing a suitable phase shift instead of negating the voltage.

It will be interesting to explore the topological phases that might appear in such electrical networks. For example, the diamond chain is also known to have symmetry-protected edge modes when the on-site potentials are all equal on all sites. This can easily be realized by attaching additional inductors to the U_n, V_n nodes and to the ground and may be an interesting extension for further studies. Moreover, as already discussed previously, the present setting offers numerous additional opportunities for exploring the interplay of CLS-connected (compact) localization with impurity-induced Anderson localization, as was recently explored in photonic systems [64]. On the other hand, for sufficiently large voltage excitations, in which elements such as the capacitors may operate in nonlinear capacitance-voltage-dependent regimes [65], it is natural to explore the generalization of the configurations considered here to the nonlinear regime. The latter and the nature of the associated excitations (compact or exponentially localized for different bands) and of the transport properties of the nonlinear lattice are particularly interesting directions in their own right.

ACKNOWLEDGMENTS

Financial support from the Institute for Basic Science (IBS) in the Republic of Korea through Project No. IBS-R024-D1 is acknowledged (S.F.). This material is partially based on work supported by the U.S. National Science Foundation under Awards No. PHY-2110030, No. DMS-2204702,

and No. PHY-2408988 (P.G.K.). This research was partly conducted while P.G.K. was visiting the Okinawa Institute of Science and Technology (OIST) through the Theoretical Sciences Visiting Program (TSVP). This work was also supported by a grant from the Simons Foundation (Grant No. SFI-MPS-SFM-00011048, P.G.K.).

The authors declare no conflict of interest.

DATA AVAILABILITY

The data that support the findings of this article are not publicly available. The data are available from the authors upon reasonable request.

- [1] D. Leykam, S. Flach, O. Bahat-Treidel, and A. S. Desyatnikov, Flat band states: Disorder and nonlinearity, *Phys. Rev. B* **88**, 224203 (2013).
- [2] D. Leykam, A. Andreanov, and S. Flach, Artificial flat band systems: From lattice models to experiments, *Adv. Phys.: X* **3**, 1473052 (2018).
- [3] C. Danieli, A. Andreanov, D. Leykam, and S. Flach, Flat band fine-tuning and its photonic applications, *Nanophotonics* **13**, 3925 (2024).
- [4] J.-W. Rhim and B.-J. Yang, Singular flat bands, *Adv. Phys.: X* **6**, 1901606 (2021).
- [5] Y. Nakata, T. Okada, T. Nakanishi, and M. Kitano, Observation of flat band for terahertz spoof plasmons in a metallic kagome lattice, *Phys. Rev. B* **85**, 205128 (2012).
- [6] S. Mukherjee, A. Spracklen, D. Choudhury, N. Goldman, P. Öhberg, E. Andersson, and R. R. Thomson, Observation of a localized flat-band state in a photonic Lieb lattice, *Phys. Rev. Lett.* **114**, 245504 (2015).
- [7] S. Kajiwar, Y. Urade, Y. Nakata, T. Nakanishi, and M. Kitano, Observation of a nonradiative flat band for spoof surface plasmons in a metallic Lieb lattice, *Phys. Rev. B* **93**, 075126 (2016).
- [8] R. A. Vicencio, C. Cantillano, L. Morales-Inostroza, B. Real, C. Mejía-Cortés, S. Weimann, A. Szameit, and M. I. Molina, Observation of localized states in Lieb photonic lattices, *Phys. Rev. Lett.* **114**, 245503 (2015).
- [9] H. S. Nguyen, F. Dubois, T. Deschamps, S. Cuff, A. Pardon, J.-L. Leclercq, C. Seassal, X. Letartre, and P. Viktorovitch, Symmetry breaking in photonic crystals: On-demand dispersion from flatband to Dirac cones, *Phys. Rev. Lett.* **120**, 066102 (2018).
- [10] J. Ma, J.-W. Rhim, L. Tang, S. Xia, H. Wang, X. Zheng, S. Xia, D. Song, Y. Hu, Y. Li, B.-J. Yang, D. Leykam, and Z. Chen, Direct observation of flatband loop states arising from nontrivial real-space topology, *Phys. Rev. Lett.* **124**, 183901 (2020).
- [11] F. Baboux, L. Ge, T. Jacqmin, M. Biondi, E. Galopin, A. Lemaître, L. Le Gratiet, I. Sagnes, S. Schmidt, H. E. Türeci, A. Amo, and J. Bloch, Bosonic condensation and disorder-induced localization in a flat band, *Phys. Rev. Lett.* **116**, 066402 (2016).
- [12] N. Masumoto, N. Y. Kim, T. Byrnes, K. Kusudo, A. Löffler, S. Höfling, A. Forchel, and Y. Yamamoto, Exciton-polariton condensates with flat bands in a two-dimensional kagome lattice, *New J. Phys.* **14**, 065002 (2012).
- [13] W. Zhang, H. Wang, H. Sun, and X. Zhang, Non-Abelian inverse Anderson transitions, *Phys. Rev. Lett.* **130**, 206401 (2023).
- [14] H. Wang, W. Zhang, H. Sun, and X. Zhang, Observation of inverse Anderson transitions in Aharonov-Bohm topoelectrical circuits, *Phys. Rev. B* **106**, 104203 (2022).
- [15] H. Wang, B. Yang, W. Xu, Y. Fan, Q. Guo, Z. Zhu, and C. T. Chan, Highly degenerate photonic flat bands arising from complete graph configurations, *Phys. Rev. A* **100**, 043841 (2019).
- [16] X. Zhou, W. Zhang, H. Sun, and X. Zhang, Observation of flat-band localization and topological edge states induced by effective strong interactions in electrical circuit networks, *Phys. Rev. B* **107**, 035152 (2023).
- [17] C. Chase-Mayoral, L. Q. English, N. Lape, Y. Kim, S. Lee, A. Andreanov, S. Flach, and P. G. Kevrekidis, Compact localized states in electric circuit flat-band lattices, *Phys. Rev. B* **109**, 075430 (2024).
- [18] M. Tovmasyan, E. P. L. van Nieuwenburg, and S. D. Huber, Geometry-induced pair condensation, *Phys. Rev. B* **88**, 220510(R) (2013).
- [19] S. Takayoshi, H. Katsura, N. Watanabe, and H. Aoki, Phase diagram and pair Tomonaga-Luttinger liquid in a Bose-Hubbard model with flat bands, *Phys. Rev. A* **88**, 063613 (2013).
- [20] G. Pelegrí, A. M. Marques, V. Ahufinger, J. Mompart, and R. G. Dias, Interaction-induced topological properties of two bosons in flat-band systems, *Phys. Rev. Res.* **2**, 033267 (2020).
- [21] Y. Kuno, T. Mizoguchi, and Y. Hatsugai, Interaction-induced doublons and embedded topological subspace in a complete flat-band system, *Phys. Rev. A* **102**, 063325 (2020).
- [22] E. Nicolau, A. M. Marques, R. G. Dias, J. Mompart, and V. Ahufinger, Many-body Aharonov-Bohm caging in a lattice of rings, *Phys. Rev. A* **107**, 023305 (2023).
- [23] Y. Kuno, T. Mizoguchi, and Y. Hatsugai, Flat band quantum scar, *Phys. Rev. B* **102**, 241115(R) (2020).
- [24] C. Danieli, A. Andreanov, and S. Flach, Many-body flatband localization, *Phys. Rev. B* **102**, 041116(R) (2020).
- [25] I. Vakulchyk, C. Danieli, A. Andreanov, and S. Flach, Heat percolation in many-body flat-band localizing systems, *Phys. Rev. B* **104**, 144207 (2021).
- [26] C. Danieli, A. Andreanov, and S. Flach, Many-body localization transition from flat-band fine tuning, *Phys. Rev. B* **105**, L041113 (2022).
- [27] S. Tilleke, M. Daumann, and T. Dahm, Nearest neighbour particle-particle interaction in fermionic quasi one-dimensional flat band lattices, *Z. Naturforsch. A* **75**, 393 (2020).
- [28] M. Goda, S. Nishino, and H. Matsuda, Inverse Anderson transition caused by flatbands, *Phys. Rev. Lett.* **96**, 126401 (2006).
- [29] T. Čadež, Y. Kim, A. Andreanov, and S. Flach, Metal-insulator transition in infinitesimally weakly disordered flat bands, *Phys. Rev. B* **104**, L180201 (2021).
- [30] Y. Kim, T. Čadež, A. Andreanov, and S. Flach, Flat band induced metal-insulator transitions for weak magnetic flux and spin-orbit disorder, *Phys. Rev. B* **107**, 174202 (2023).
- [31] S. Lee, A. Andreanov, and S. Flach, Critical-to-insulator transitions and fractality edges in perturbed flat bands, *Phys. Rev. B* **107**, 014204 (2023).
- [32] S. Lee, S. Flach, and A. Andreanov, Critical state generators from perturbed flatbands, *Chaos* **33**, 073125 (2023).

- [33] J.-W. Rhim, K. Kim, and B.-J. Yang, Quantum distance and anomalous Landau levels of flat bands, *Nature (London)* **584**, 59 (2020).
- [34] C. Danieli, A. Andreanov, T. Mithun, and S. Flach, Nonlinear caging in all-bands-flat lattices, *Phys. Rev. B* **104**, 085131 (2021).
- [35] C. Danieli, A. Maluckov, and S. Flach, Compact discrete breathers on flat-band networks, *Low Temp. Phys.* **44**, 678 (2018).
- [36] R. A. Vicencio and M. Johansson, Discrete flat-band solitons in the kagome lattice, *Phys. Rev. A* **87**, 061803(R) (2013).
- [37] W. Maimaiti, A. Andreanov, H. C. Park, O. Gendelman, and S. Flach, Compact localized states and flat-band generators in one dimension, *Phys. Rev. B* **95**, 115135 (2017).
- [38] Y. Hwang, J.-W. Rhim, and B.-J. Yang, General construction of flat bands with and without band crossings based on wave function singularity, *Phys. Rev. B* **104**, 085144 (2021).
- [39] A. Graf and F. Piéchon, Designing flat-band tight-binding models with tunable multifold band touching points, *Phys. Rev. B* **104**, 195128 (2021).
- [40] J.-W. Ryu, A. Andreanov, H. C. Park, and J.-H. Han, Orthogonal flatbands in Hamiltonians with local symmetry, *J. Phys. A* **57**, 495301 (2024).
- [41] C. V. Morfonios, M. Röntgen, M. Pyzh, and P. Schmelcher, Flat bands by latent symmetry, *Phys. Rev. B* **104**, 035105 (2021).
- [42] S. Flach, D. Leykam, J. D. Bodyfelt, P. Matthies, and A. S. Desyatnikov, Detangling flat bands into Fano lattices, *Europhys. Lett.* **105**, 30001 (2014).
- [43] L. Morales-Inostroza and R. A. Vicencio, Simple method to construct flat-band lattices, *Phys. Rev. A* **94**, 043831 (2016).
- [44] Z. Li, J. Zhuang, L. Wang, H. Feng, Q. Gao, X. Xu, W. Hao, X. Wang, C. Zhang, K. Wu, S. X. Dou, L. Chen, Z. Hu, and Y. Du, Realization of flat band with possible nontrivial topology in electronic kagome lattice, *Sci. Adv.* **4**, aau4511 (2018).
- [45] C. H. Lee, S. Imhof, C. Berger, F. Bayer, J. Brehm, L. W. Molenkamp, T. Kiessling, and R. Thomale, Topoelectrical circuits, *Commun. Phys.* **1**, 39 (2018).
- [46] H. Sahin, M. Jalil, and C. H. Lee, Topoelectrical circuits—Recent experimental advances and developments, *APL Electron. Devices* **1**, 021503 (2025).
- [47] L. Q. English, F. Palmero, P. Candiani, J. Cuevas, R. Carretero-González, P. G. Kevrekidis, and A. J. Sievers, Generation of localized modes in an electrical lattice using subharmonic driving, *Phys. Rev. Lett.* **108**, 084101 (2012).
- [48] L. Q. English, F. Palmero, A. J. Sievers, P. G. Kevrekidis, and D. H. Barnak, Traveling and stationary intrinsic localized modes and their spatial control in electrical lattices, *Phys. Rev. E* **81**, 046605 (2010).
- [49] X.-L. Chen, S. Abdoukary, P. G. Kevrekidis, and L. Q. English, Resonant localized modes in electrical lattices with second-neighbor coupling, *Phys. Rev. E* **98**, 052201 (2018).
- [50] M. Ezawa, Non-Hermitian higher-order topological states in nonreciprocal and reciprocal systems with their electric-circuit realization, *Phys. Rev. B* **99**, 201411(R) (2019).
- [51] T. Kotwal, F. Moseley, A. Stegmaier, S. Imhof, H. Brand, T. Kießling, R. Thomale, H. Ronellenfitsch, and J. Dunkel, Active topoelectrical circuits, *Proc. Natl. Acad. Sci. USA* **118**, e2106411118 (2021).
- [52] A. R. Kolovsky, P. S. Muraev, and S. Flach, Conductance transition with interacting bosons in an Aharonov-Bohm cage, *Phys. Rev. A* **108**, L010201 (2023).
- [53] M. Kremer, I. Petrides, E. Meyer, M. Heinrich, O. Zilberberg, and A. Szameit, A square-root topological insulator with non-quantized indices realized with photonic Aharonov-Bohm cages, *Nat. Commun.* **11**, 907 (2020).
- [54] H. Song, R. Zhang, and V. Van, Observation of compact localized states in synthetic Floquet-Lieb topological photonic lattices, *Commun. Phys.* **8**, 219 (2025).
- [55] D. Román-Cortés, M. Mazanov, R. A. Vicencio, and M. A. Gorlach, Observation of invisibility angle and flat band physics in dipolar photonic lattices, *Nano Lett.* **25**, 4291 (2025).
- [56] J. Yang, Y. Li, Y. Yang, X. Xie, Z. Zhang, J. Yuan, H. Cai, D.-W. Wang, and F. Gao, Realization of all-band-flat photonic lattices, *Nat. Commun.* **15**, 1484 (2024).
- [57] J. G. C. Martinez, C. S. Chiu, B. M. Smitham, and A. A. Houck, Interaction-induced escape from an Aharonov-Bohm cage, *Sci. Adv.* **9**, eadj7195 (2023).
- [58] J. Vidal, R. Mosseri, and B. Douçot, Aharonov-Bohm cages in two-dimensional structures, *Phys. Rev. Lett.* **81**, 5888 (1998).
- [59] J. Vidal, B. Douçot, R. Mosseri, and P. Butaud, Interaction induced delocalization for two particles in a periodic potential, *Phys. Rev. Lett.* **85**, 3906 (2000).
- [60] B. Douçot and J. Vidal, Pairing of Cooper pairs in a fully frustrated Josephson-junction chain, *Phys. Rev. Lett.* **88**, 227005 (2002).
- [61] This resistance does not affect the op-amp if it is ideal. In practice, the impedance difference at two inputs creates a small input bias voltage between two inputs: $V_B = I_B/(R_- - R_G)$, distorting the output voltage. To mitigate this effect, R_G is attached at the + input, that is, $R_G = R_-$, i.e., $R_G = R/2$. See Ref. [66] for technical details. Furthermore, note that R should not be too large because then parasitic capacitance at the inverting input induces an unwanted $\pi/2$ phase shift and large noise at high frequency.
- [62] D. Călugăru, A. Chew, L. Elcoro, Y. Xu, N. Regnault, Z.-D. Song, and B. A. Bernevig, General construction and topological classification of crystalline flat bands, *Nat. Phys.* **18**, 185 (2022).
- [63] M. I. Molina, L. Q. English, M.-H. Chang, and P. G. Kevrekidis, Linear impurity modes in an electrical lattice: Theory and experiment, *Phys. Rev. E* **100**, 062114 (2019).
- [64] E. J. Dresselhaus, A. Avdoshkin, Z. Jia, M. Secli, B. Kante, and J. E. Moore, A tale of two localizations: Coexistence of flat bands and Anderson localization in a photonics-inspired amorphous system, *Phys. Rev. B* **112**, 064202 (2025).
- [65] M. Remoissenet, *Waves Called Solitons: Concepts and Experiments*, 3rd ed., Advanced Texts in Physics (Springer, Berlin, 1999).
- [66] Texas Instruments, AN-20: An applications guide for Op Amps, revision C, Application Report SNOA621C, Texas Instruments (2013) [originally published February 1969], <https://www.ti.com/lit/an/snoa621c/snoa621c.pdf>.